J Biochem Tech (2020) Special Issue (1): 161-174
ISSN: 0974-2328

An Analysis of the Natural Circulation Pattern of Super Critical Water Reactor Based on Drawing Stability Map

Milad Mansouri Rad

Received: 24 July 2019 / Received in revised form: 10 November 2019, Accepted: 14 November 2019, Published online: 25 January 2020

Abstract

Super Critical Water Reactor (SCWR) is one of the six types of nuclear reactors proposed by Generation 4 International Forum (GIF), whose technology is based on light water reactors. SCWRs are designed to remove heat from the core using the natural heat-circulation system, usually done by active pumps. This makes the reactors safer. The computational model starts by determining the survival equations (mass, energy and momentum) considered for the nodes. In the stability analysis model and drawing the stability map, these equations are first made linear and then are made dimensionless for better examination. Stability is solved by examining the system response to the created disruption. Stability maps are obtained for an operational period to provide a deeper look towards the inconsistencies in the system. A parametric study was conducted to examine the effect of different design parameters. The rising length is considered an important design parameter, as the increase in length makes the system unstable. In other words, it increases the mass flux rate. One has to consider the interaction between a stable system and a mass flux rate. We found that stability is reduced by increasing the wall cross-section.

Key words: SCWR, Instability model, Survival equations

Introduction

Many studies have been conducted on the stability of water cycles in boiling-water reactors in recent decades. The most recognizable feature of natural systems is their sensitivity to work conditions and their tendency towards instability is usually due to the flexible pairing between the flow and the temperature fields. The lower turnover rate, compared with the cycles containing the primary circulator, as well as other features such as momentum and viscosity (considering inertial effects insignificant). Accordingly, the flow field is an implicit function of many parameters that affect the geometry of the cycle, boundary conditions, and spatial conditions. Thus, all effective parameters have to be detected and evaluated well in a two-phase flow system, like boiling-water reactors. Various instability types have been classified by Boure (1973). Wave density fluctuations are as one of the most common instabilities in two-phase flow systems (Colombo et al., 2012) and widely examined in laboratories and studies. For instance, Van Braget (1998) conducted some studies on stability problems along with cooling the core with the natural circulation system of the boiling-water reactor. They did a parametric study to examine the effect of different parameters on water circulation. As in the super-critical circulation of water significant density drop occurs compared to the two-phase flow system, there is an underlying thought that there are instability fluctuations in the density wave in these super-critical systems, except that there is just one phase here. The study examines the response of the super-critical water circulation system to disruptions and checks whether the instabilities in boiling water reactors exist either as well.

It has been shown that system stability is related to design parameters and various operating conditions like power, flow rate, input temperature, and geometry (Van Braget, 1998). The operating conditions of a light water reactor can be summarized by two dimensionless variables. One is usually as a ratio that expresses heat and mass flow, and the other is a value for the core temperature input. Accordingly, these values can be used as axes of stability and operational stability plan. The boundary between unstable and stable regions on such maps is known as “neutral stability boundary”.

Survival equations for the stability map review system

The equations start by writing the mass equation, then we go to the energy equation and eventually we finish the equations by writing the momentum equation. Here, the mass and energy equations are written for each component, including the heater (the core), riser, buffer (coolant) and dropdown, and the momentum equation is integrated throughout the entire system.

Milad Mansouri Rad

Faculty of Physics and Energy Engineering, Amirkabir University of Technology (Tehran Polytechnic)

Survival equations for the super-critical model

In the subcritical model, the core only contains one node. Thus, the node length is constant. It is assumed that the core enthalpy linearly increases from the enthalpy of the input to the enthalpy of the output. The output enthalpy depends on-time output, input enthalpy, and core strength. This makes the zero-node density, contrary to the super-critical model, time-dependent. In this model, water reaches the quasi-critical point in the core, so the core is divided into two nodes. The base math structure for this loop is similar to the sub-critical model. This section presents a more complete formulation of survival equations. Equations that do not contribute to the stability problem are eliminated. Four mass equations below are established for 4 water loop nodes and the dropdown mass equation is eliminated. The length of the zero and one node of the core are animated. The total length of the core is constant. In addition, unlike the sub-critical model, the enthalpy (zero enthalpy) is constant. It is assumed that the enthalpy increases linearly from the input enthalpy to the enthalpy of the quasi-critical point, and we consider the mean of these two points as the zero enthalpy. Zero density is constant as well.

$$M_0: A\rho_0 \frac{d}{dt} L_0 = W_0 - W_{pc} \quad (1)$$

$$M_1: A \frac{d}{dt} \rho_1 L_1 = W_{pc} - W_1 \quad (2)$$

$$M_R: AL_R \frac{d}{dt} \rho_R = W_1 - W_R \quad (3)$$

$$M_B: \rho_{IN} \frac{d}{dt} V_B = W_R - W_0 \quad (4)$$

The heath of the core nodes is proportional to their length. Dropdown energy and buffers equations have been eliminated. The new equations introduce the two enthalpy variables of node 1 and new rising enthalpy.

Power is distributed uniformly throughout the core, so they are distributed at the same rate for each node.

$$\underline{E_0}: A\rho_0 H_0 \frac{d}{dt} L_0 = W_0 H_{in} - W_{pc} h_{pc} + \frac{Nu_0 \lambda_f}{D_H} P_{in} L_0 (T_{w,0} - T_0) \quad (5)$$

$$\underline{E_1}: A \frac{d}{dt} \rho_1 L_1 H_1 = W_{pc} h_{pc} - W_1 H_1 + \frac{Nu_1 \lambda_f}{D_H} P_{in} L_1 (T_{w,1} - T_1)$$

$$\underline{E_{w_0}}: \rho_w c_{p,w} A_w \frac{d}{dt} L_0 T_{w,0} = Q \frac{L_0}{L} - \frac{Nu_0 \lambda_f}{D_H} P_{in} L_0 (T_{w,0} - T_0) + \frac{2\lambda_w}{L} A_w (T_{w,1} - T_{w,0}) \quad (6)$$

$$\underline{E_{w_1}}: \rho_w c_{p,w} A_w \frac{d}{dt} L_1 T_{w,1} = Q \frac{L_1}{L} - \frac{Nu_1 \lambda_f}{D_H} P_{in} L_1 (T_{w,1} - T_1) - \frac{2\lambda_w}{L} A_w (T_{w,1} - T_{w,0})$$

$$E_R: AL_R \frac{d}{dt} \rho_R H_R = W_1 H_1 - W_R H_R \quad (7)$$

Energy equations for wall nodes are similar to the sub-critical model. The section related to the power component (Q) contains heat corresponding to the length of nodes, and the parts including Nusselt number, related to heat, flow between the wall nodes and the corresponding core nodes. An additional part must exist for the survival equation, which is related to the heat exchange between the wall nodes. This exchange of heat occurs during thermal conduction as follows.

$$q = q''^{A_w} = -\lambda_w \nabla T A_w \quad (8)$$

Landau coefficient (assumed constant) is the thermal conductivity of the wall.
The temperature gradient is written as follows.

$$\nabla T = \frac{\Delta T}{\Delta z} \quad (9)$$

As it is necessary to consider a distance between the wall nodes as a distance variation (delta-z), for simplicity, half the total length of the nodes is selected. In this case, the temperature gradient is written as follows.

$$\nabla T = \frac{2\Delta T}{L} \quad (10)$$

The heat exchange between the wall nodes is added to the energy equations (6) and (5). This part is:

(11) $\frac{2\lambda_w}{L} A_w\left(T_{w,1} - T_{w,0}\right)$

This system can be made a little simpler. We know that the length of the nodes, one and zero, are collectively constant and the size of the lengths does not depend on time itself.
We can combine the energy equations for the zero and one nodes into an energy equation.

$$\underline{E_1}:\left(\rho_1 H_1 - \rho_0 H_0\right) A \frac{d}{dt} L_1 + A L_1 \frac{d}{dt} \rho_1 H_1 \quad (12)$$
$$= W_0 H_{in} - W_1 H_1 \ldots + \frac{Nu_0 \lambda_f}{D_H} P_{in}(1 - L_1)\left(T_{w,0} - T_0\right) + \frac{Nu_1 \lambda_f}{D_H} P_{in} L_1 \left(T_{w,1} - T_1\right)$$

Finally, we write the momentum equations that are integrated throughout the cycle.
(13)

$$I: A \frac{d}{dt} W_0 L_0 + A \frac{d}{dt} W_1 L_1 + A L_R \frac{d}{dt} W_R + \frac{d}{dt} V_B W_0 + A L_D \frac{d}{dt} W_0 = \quad (13)$$
$$-\frac{1}{2}\left(\frac{f_0 L_0}{D_h} + K_0\right)\frac{W_0^2}{\rho_0} - \frac{1}{2}\left(\frac{f_1 L_1}{D_h} + K_1\right)\frac{W_1^2}{\rho_1} - \frac{1}{2}\left(\frac{f_R L_R}{D_h} + K_R\right)\frac{W_R^2}{\rho_R}$$
$$-\frac{1}{2}\left(\frac{f_D L_D}{D_h} + K_D\right)\frac{W_0^2}{\rho_{IN}} \ldots - A^2 g \rho_0 L_0 - A^2 g \rho_1 L_1 - A^2 g \rho_R L_R + A^2 g \rho_{IN} L_D$$

The equation for the static mass flow rate for this model is written as follows.

$$\bar{W}^2 = gA^2 \frac{\rho_{IN} L_D - \rho_0 \bar{L}_0 - \bar{\rho}_1 (\bar{L}_1 + L_R)}{\frac{1}{2}\left(\frac{f_0 \bar{L}_0}{D_h} + K_0\right)\frac{1}{\rho_0} + \frac{1}{2}\left(\frac{f_D L_D}{D_h} + K_D\right)\frac{1}{P_{IN}} + \frac{1}{2}\left(\frac{f_1 \bar{L}_1}{D_h} + K_1 + \frac{f_R L_R}{D_h} + K_R\right)\frac{1}{\rho_1}} \quad (14)$$

Using the equations below, one can reduce the number and complexity of equations and variables.

$$W_{pc} = W_0 \frac{H_{IN}}{h_{pc}} + \frac{Q}{h_{pc}} \frac{L_0}{L} - A\rho_0 \frac{H_0}{h_{pc}} \frac{d}{dt} L_0 \quad (15)$$

The first equation modes that the time derivative of the length of the zero-one nodes is equal (with a negative sign). This equation is in fact a result of Equation (2). Mass flux rate of a quasi-critical point can be expressed in other variables, as this variable does not have any time-derivation in any equation. This eliminates an equation and a variable. Moreover, densities are replaced by the equation of mode equation. The mass equation of the buffer compartment is embedded in the momentum equation (as in the previous model). Thus, the buffer variable and the mass equation of the buffer are eliminated. Overall, by writing the equations and reducing them to the possible extent, we reach the following equations.

$$M_0 \quad M_1 \quad M_R \quad E_1 \quad E_R \quad l \quad E_{w_0} \quad E_{w_1}$$

In this study, we made the transfer equations to describe the working conditions of the dimensionless parameters that were made. This will make it easier to examine the behavior of a different structure.
We show the stable mode variables for the x parameter using $\bar{X}$, for disruption $\underline{X}$ and the dimensionless variable $\tilde{x}$.
Bear in mind that we will subtitude several friction coefficients to demonstrate the changes in variables .
The method used to calculate friction between a wall and a flow is a combination of several isothermal friction factor relationships. Which one to use depends on the Reynolds number at that point in the simulation. The relationships used are illustrated below. All of these equations accurately describe the subcritical flow at different intervals of their rhinoceros. In analyzing the thermohydraulic properties, we use Blasius and McAdams relations and Feng, Yamshita and Popov equations are used for stability analysis
Three usable relationships were selected for further evaluation. Feng, Yamashita and Popov relations. These choices are based on their performance in laboratory investigations and considering the variables required in the model.

The friction factor relationship produced by Feng is a combination of existing data and relationships. The goal was to reduce errors and to achieve a general usability relationship.

$$f=f_{iso,b}\left(\frac{\mu_w}{\mu_b}\right)^{0.49\left(\frac{\rho f}{\rho pc}\right)^{1.31}}$$

$$f_{iso,b}=1.613[0.234(\ln\ (\left(\frac{\epsilon}{D}\right)^{1.1007}-\frac{60.525}{Re^{1.1105}}+\frac{56.201}{Re^{1.0712}}\right)]^{-2}$$

Yamshita conducted an in vitro study of the friction factor - AR22 - which flowed in a vertical heated tube with a uniform cross-sectional area of 404 mm in diameter. This relation also has a supercritical part that, if the wall relative temperature and volume are zero, the ratio of the fruit wall and the volume fruit is equal to 1.

$$f=f_{iso,b}\left(\frac{\mu_w}{\mu_b}\right)^{0.72}$$

$$f_{iso,b}=\frac{0.314}{0.7-1.65\log Re+(\log Re)^2}$$

Popov acquired a relationship with the study of supercritical carbon dioxide turbulent flow. The volumetric isobar friction factor was obtained using the Filonenko equation. The supercritical part in this respect is based on changes in density. The two previous relationships were based on adhesion. This relation also has a supercritical part in which, if the relative temperature between the wall and the volume is zero, the specified density ratio will be 1

$$f=f_{iso,b}\left(\frac{\rho f}{\rho b}\right)^{0.74}$$

$$f_{iso,b}=(0.79\ln Re-1.64)^{-2}$$

Dimensionless survival equations for the super-critical model

In this section, dimensionless survival equations are given for the survival of mass, energy, and momentum. As before, the mass equation is initially given, then energy and finally the momentum.

$$E_1:\underline{L_1}\frac{d}{dt}\underline{\rho_1 H_1}+\left(\underline{\rho_1 H_1}-\underline{\rho_0 H_0}\right)\frac{d}{dt}\underline{L_1}=\underline{W_0 H_{in}}-\underline{W_1 H_1}\ldots$$

$$+\underline{Nu_0\lambda_{f0}^{0.34}}\frac{\underline{P_{in}}\left(1-\underline{L_1}\right)}{\underline{D_H}}\left(\underline{T_{w,0}}-\underline{T_{pc}}-\underline{\alpha_0}\left(\underline{H_0}-\underline{h_{pc}}\right)^2-\frac{1}{\underline{c_p.pc}}\left(\underline{H_0}-\underline{h_{pc}}\right)\right)\ldots \quad (16)$$

$$+\underline{Nu_1\lambda_{f1}^{0.34}}\frac{\underline{P_{in}L_1}}{\underline{D_H}}\left(\underline{T_{w,1}}-\underline{T_{pc}}-\underline{\alpha_1}\left(\underline{H_1}-\underline{h_{pc}}\right)^2-\frac{1}{\underline{c_p pc}}\left(\underline{H_1}-\underline{h_{pc}}\right)\right)$$

$$\underset{\sim}{E}_R:\underset{\sim}{L}_R\frac{d}{dt}\underset{\sim}{\rho}_R\underset{\sim}{H}_R=\underset{\sim}{W}_1\underset{\sim}{H}_1-\underset{\sim}{W}_R\underset{\sim}{H}_R \quad (17)$$

$$\underline{E_{w0}}:\underline{\rho_w}\underline{c_{p,w}}\underline{A_w}(1-\underline{L_1})\frac{d}{dt}\underline{T_{w,0}}-\underline{\rho_w}\underline{c_{p,w}}\underline{A_w}\underline{T_{w,0}}\frac{d}{dt}\underline{L_1}$$

$$=1-L_1\ldots-\underline{Nu_0\lambda_{f0}^{0.34}}\frac{\underline{P_{in}}(1-\underline{L_1})}{\underline{D_H}}\left(\underline{T_{w,0}}-\underline{T_{pc}}-\underline{\alpha_0}\left(\underline{H_0}-\underline{h_{pc}}\right)^2-\frac{1}{\underline{c_p.pc}}\left(\underline{H_0}-\underline{h_{pc}}\right)\right)\ldots \quad (18)$$

$$+\underline{\lambda_w A_w}(\underline{T_{w,1}}-\underline{T_{w,0}})$$

$$\underline{E_{w1}}: \underline{\rho_w c_{p,w} A_w T_{w,1}} \frac{d}{d\underline{t}} \underline{L_1} + \underline{\rho_w c_{p,w} A_w L_1} \frac{d}{d\underline{t}} \underline{T_{w,1}} = L_1 \ldots - \underline{Nu_1 \lambda_{f1}^{0.34}} \frac{\underline{P_{in} L_1}}{\underline{D_H}} \left(\underline{T_{w,1}} - \underline{T_{pc}} - \underline{\alpha_1} \left(\underline{H_1} - \underline{h_{pc}} \right)^2 - \frac{1}{\underline{c_{p.pc}}} \left(\underline{H_1} - \underline{h_{pc}} \right) \right) \ldots -$$

$$2\underline{\lambda_w A_w} (\underline{T_{w,1}} - \underline{T_{w,0}}) \quad (19)$$

$$\underset{\sim}{I}: \underset{\sim}{W_0} \frac{d}{d\underset{\sim}{t}} \underset{\sim}{L_1} + (1 - \underset{\sim}{L_1}) \frac{d}{d\underset{\sim}{t}} \underset{\sim}{W_0} + \frac{d}{d\underset{\sim}{t}} \underset{\sim}{W_1} \underset{\sim}{L_1} + \underset{\sim}{L_R} \frac{d}{d\underset{\sim}{t}} \underset{\sim}{W_R} + \underset{\sim}{V_B} \frac{d}{d\underset{\sim}{t}} \underset{\sim}{W_0} + \underset{\sim}{L_D} \frac{d}{d\underset{\sim}{t}} \underset{\sim}{W_0} = -\underset{\sim}{W_0} \left(\frac{\underset{\sim}{W_R} - \underset{\sim}{W_0}}{\underset{\sim}{P_{IN}}} \right) \ldots$$

$$- \frac{1}{2} \left(\frac{\underset{\sim}{f_0} \underset{\sim}{L_0}}{\underset{\sim}{D_h}} + K_0 \right) \frac{\underset{\sim}{W_0^2}}{\underset{\sim}{\rho_0}} - \frac{1}{2} \left(\frac{\underset{\sim}{f_1} \underset{\sim}{L_1}}{\underset{\sim}{D_h}} + K_1 \right) \frac{\underset{\sim}{W_1^2}}{\underset{\sim}{\rho_1}} - \frac{1}{2} \left(\frac{\underset{\sim}{f_R} \underset{\sim}{L_R}}{\underset{\sim}{D_h}} + K_R \right) \frac{\underset{\sim}{W_R^2}}{\underset{\sim}{P_P}} - \frac{1}{2} \left(\frac{\underset{\sim}{f_D} \underset{\sim}{L_D}}{\underset{\sim}{D_h}} + K_R \right) \frac{\underset{\sim}{W_0^2}}{\underset{\sim}{\rho_{IN}}} \ldots \quad (20)$$

$$- \frac{\underset{\sim}{\rho_0} \underset{\sim}{L_0}}{N_{Fr}} - \frac{\underset{\sim}{\rho_1} \underset{\sim}{L_1}}{N_{Fr}} - \frac{\underset{\sim}{\rho_R} \underset{\sim}{L_R}}{N_{Fr}} + \frac{\underset{\sim}{\rho_{LN}} \underset{\sim}{L_D}}{N_{Fr}}$$

Stability characteristics

Dimensionless numbers

The stability map is obtained for two operating conditions, input temperature and thermal power. As the circulation system is normal, the thermal power actually represents the mass flux because the mass flux is no longer controlled by the pump. To compare the stability maps for different stops, we introduce two dimensionless numbers representing these operating conditions expressed as:

(32) $$N_{sub} = 1 - \frac{H_{IN}}{h_{pc}}$$

(33) $$N_{\Delta h} = \frac{Q}{\bar{w} h_{pc}}$$

N_{sub} is a cold number (sub-cool). It is a value for the input temperature (specific enthalpy input). This number decreases with increasing temperature (enthalpy). It is assumed that the input enthalpy does not exceed the quasi-critical enthalpy at any $N_{\Delta h}$ time of the operation although there is no physical mechanism to prevent it from doing so. In addition, as the negative enthalpy is non-physical and has no meaning, this number cannot be larger than one. The change number is quasi-phase and a value to increase the enthalpy in the core. Contrary to the conditions in compulsory systems where mass flux is dictated by pumps, this mass flux reaches a value as a result of thermal power.

Obtaining transient mode values

The problem of mass flux stability

The study has determined the magnitudes and stability conditions using the obtained graphs for mass flux under different hydraulic pressure conditions and diameters. The problem of the mass flux stability is determined using the conditions of the initial values and boundary conditions (Vijayan et al., 2010). Boundary conditions have been described in the stable-mode solution methods section, and the permanent mode solution is used as an initial condition for transient predictions. Then, the time-dependent survival equations are solved to determine the transient response. The transient response at the selected operating point shows stable, unstable, or neutral-stable condition (Yu et al., 2011).

Solving transient mode

This type of solution is used only in the stability map analysis. Time transformation is shown by the following matrix form.

$$A \frac{d}{dt} \vec{x} = B \vec{x} \quad (34)$$

A and B are the matrices of the coefficients for the time derivatives of the variables and the variables themselves. The matrices of the coefficients are given in Appendix (b). In the supercritical model, the matrices are 5*5 (5) and the linear equation (5) is a time dependent variable. In this case, each entry is related to one variable of an equation and in the super-critical model, this size reaches 8*8. The matrix of coefficients shows linearized equations. $\vec{x}$ vector contains disruption variables. Solving this vector matrix system is as $\vec{x} =$

$\sum_{i=1}^{n} c_i \vec{v}_i e^{\lambda_i t}$ where v_l is the i-th specific vector of the matrix M_1, whose components, range and phase changes show the i-th underlying disruption. The i-th eigenvalue $\lambda_i = r_i + j\omega_i$ (should not be confused with the thermal conductivity) of M_1 matrix with two real and virtual parts. The number of solution parts is actually the number of variables in the disruption (will be according to model 5 or 8), and C_i are coefficients that depend on the system conditions at zero time.

Only the eigenvalues of λ_i are considered to examine stability. If the real part of the eigenvalue is negative, it the exponential $e^{\lambda_i t}$ is smaller than the unit and disappears over disruption time (DR <1).

If this case is applied to all exponential parts, the system will be stable.
If one of the eigenvalues has a positive real part, then at least one of the disruption variables diverges.
It affects DR> 1 and other variables. Thus, the system eventually becomes unstable.
The virtual part of an eigenvalue ω_i is the angular frequency of the i-th oscillation. Several oscillations of this case can occur at a time, but eventually, the oscillation is dominated by the largest domain (the largest positive integer in the real sector). The virtual portion of the eigenvalue, the resonant frequency of the system will be unstable.

Parametric study

Design parameters affect the supercritical water circulation of the loop stability loop. Table 1 shows an overview of the effect of different design parameters on system stability. The stabilizing effect is shown with (+) and the destabilizing effect with (-). The arrows point to the increase or decrease of the design parameter. In the following sections, we will discuss some of the parameters in detail.

Table 1: The effect of various parameters on the stability map, the stabilizing effect is shown with (+) and the destabilizing effect with (-)

Design parameter	Changes	Changes
Surface area of wall's cross-section	+	-
Thermal conductivity of the wall	+	-
Buffer volume	+	-
Rising length	-	+
Hydraulic diameter	+	-
Core length	-	+
drop coefficient of the core rate pressure	+	-
Dropdown pressure drop coefficient	+	-
Rising pressure drop coefficient	-	+

Reference case

We consider the stability map written with MATLAB code for specific design parameters as a reference and by changing the parameters, we compare the effects to the reference mode.

Table 2: Design parameters considered as reference in this thesis

Design parameters	Value
Buffer volume	10 dm3
Rising length	4.2 m
Core length	4.2 m
Hydraulic channel diameter	5.6 mm
Flow area	33.5 mm2
Core rate pressure drop coefficient	1
Dropdown pressure drop coefficient	1
Rising pressure drop coefficient	20

The line $N_{\Delta h} = N_{sub}$ is the boundary designed by the mathematical model makes a difference between the underlying and the supercritical models. On top of this boundary,

the stability is calculated with sub-critical model, and for the downstream of this boundary an overcritical model is used.
The sharp transition from the stable region to the unstable region is described in $N_{\Delta h} = N_{sub}$ with the mode equation considered (how to write the equation of mode in the mathematical code once as in the equation written in Braget 1998 and once in the form our equation is written and the results come to the same). The approximation of the mode equation considered in this thesis is relatively crude, since the mode equation is split into two different approximations separated by a quasi-critical point. At this point, the approximation is not continuous, therefore, in the line$N_{\Delta h} = N_{sub}$, the transition from a steady mode to an unstable mode is seen.

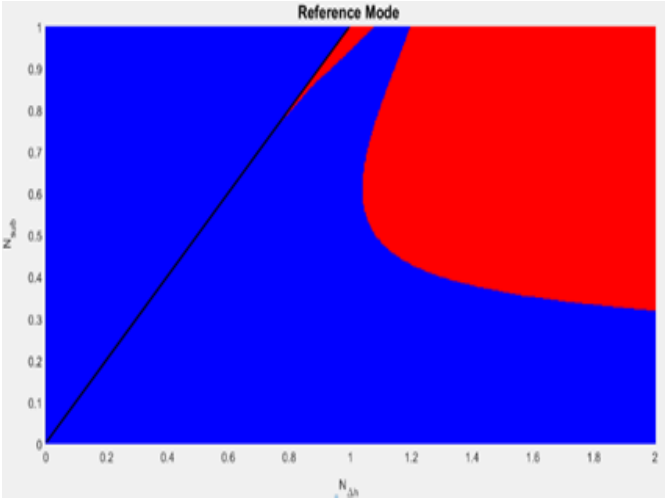

Figure 2 shows the stability map for reference mode. Red shows an unstable region and the blue a stable region. Black line shows $N_{\Delta h} = N_{sub}$.

To compare, the conditions where the cross-sectional area is as small as the cross-section of the small channel that can be ignored if the cross-sectional area of the wall relative to the cross-section of the channel is large. According to the below figures, we find that the presence of the wall has a lasting effect. The effect of the thermal inertia of the wall is also seen in the next section.
Figure 3 is the stability map (wall cross-section is one tenth of the cross-sectional area). Here, we refer to the cross-sectional area of the channel for a clearer 10-fold subject.

Area of the wall cross-section

We examined the cross-sectional area of the wall to the channel area in a wide range to determine the extent to which the cross-sectional area affects system stability. What was clarified was that there was no change in these ratios, but when the cross-sections differed significantly (about 100 times), the high sub-cooling substitutions near the line $N_{\Delta h} = N_{sub}$ decrease and create a more stable mode. However, there is no change in the right-hand region far from the quasi-critical equilibrium line. If we consider this theoretically, on a very large wall, as the thermal balance is bounded by equation$\rho_w c_{p,w} A_w L \frac{d}{dt} T_w$, the wall temperature is expected to be constant within the working time.

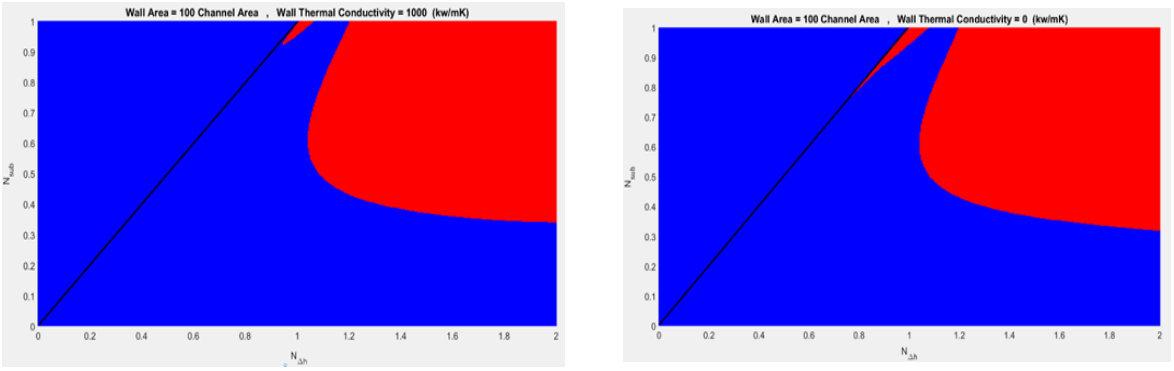

Figure 4: The stability map for reference mode (the right side of the wall cross-section is equal to the cross-sectional area of the channel 35 * 10 ** -6 while the left side has a wall cross-section of 35 * 10 ** -4)

Thermal conductivity

We want to see the effect of interaction between the nodes of the wall. This is done by a parametric study of the thermal conductivity of the wall. The behavior is examined for two different cross-sections of the wall. One cross-sectional area is equal to the channel cross-sectional area and another section 100 times larger than the cross-sectional area of the channel. The stability boundary at higher cross-sections is more sensitive to heat conduction fluctuations in the wall, because in the equilibrium equations Ew0 and Ew1, the thermal conductivity between the wall nuts is linearly related to the thermal conductivity and wall cross-section.

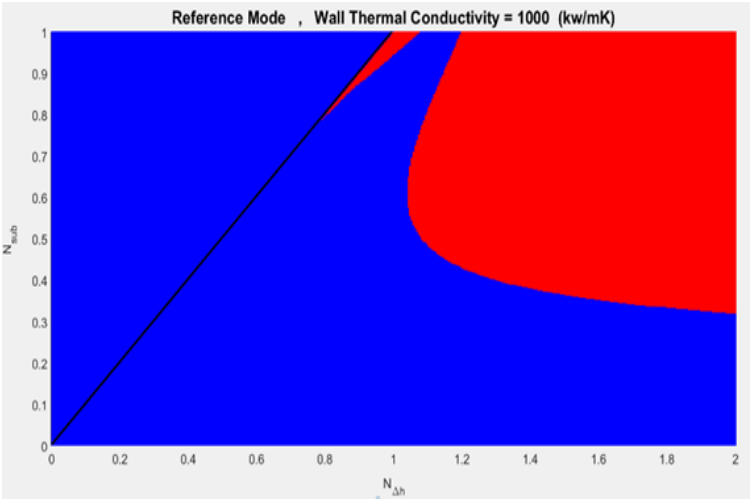

Figure 5: Stability map for the area of the cross-sectional area of the wall with the channel

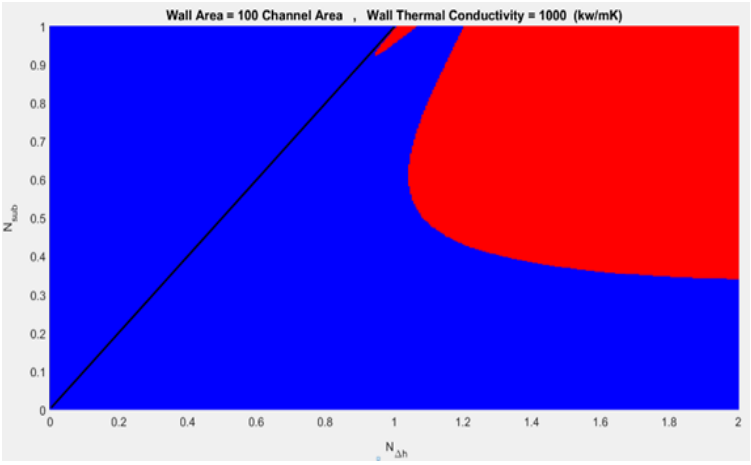

Figure 6: Stability map for the area of the cross-section 100 times the wall relative to the channel

As already stated, it was expected that the thermal conductivity would affect the surface of the upper surface more effectively. Overall, the changes are very small. A closer look at the theorem and the thermal equations Ew0 and Ew1 can show this. The weight factor of the thermal difference of the wall-to-channel heat transfer section $\frac{Nu_0\lambda_f}{D_H}P_{in}L_o$is generally around$75WK^{-1}$, whereas the axial thermal conductivity $\frac{2\lambda_w}{L}A_w$ is generally of $10^{-4}WK^{-1}$ order.

This shows that the axial thermal-conductivity can be ignored in the low and medium thermal conductivity.

Buffer volume

As the volume of the compartment increases, the range of instability becomes smaller and the system becomes more stable. Figure 7 shows two stability maps drawn for two different volumes of the buffer. We need to consider the neutral boundary to compare the maps. The neutral boundary is the boundary where the pass from a stable to unstable mode occurs. To the right and to the top of the boundary, the system is unstable and the bottom and left of that system is stable. The system becomes more stable for larger volumes of the buffer

compartment, as any growing disruption in the core or rising, in large volumes of water in the buffer disappears and becomes stable. This can be related to the linear momentum equation.

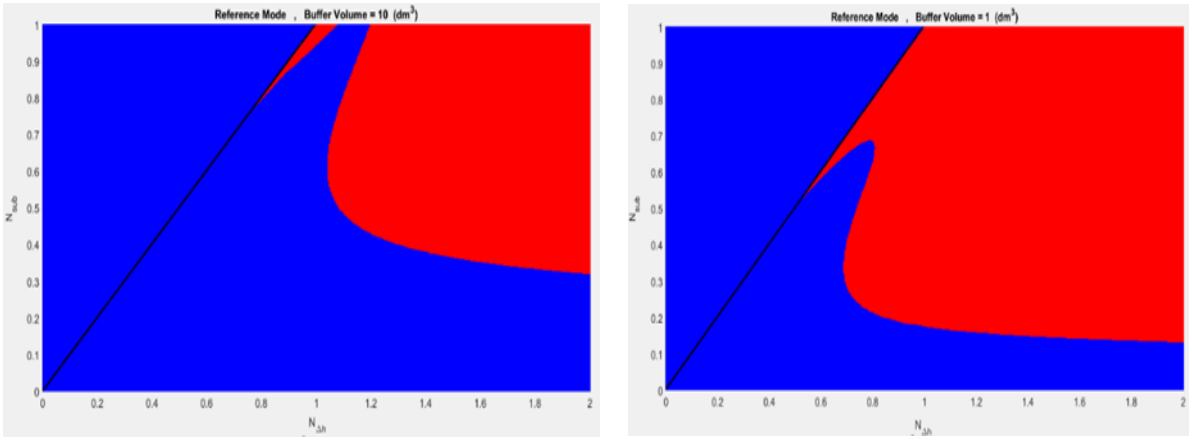

Figure 7: Stability map for different volumes of the buffer compartment

The buffer volume is made ready before $\frac{d}{d\tilde{t}} = \tilde{w}_0$ section and is proportional to the average time that the water flows into the buffer compartment. If the volume increases, mass flux rate w_0 will be severely delayed due to the mass flow rate of the input, and thus any fluctuating disruption and growth will be dissolved. Thus, the buffer compartment acts as a dimming amplifier in the loop of the water, so that the large disruption ranges are dissolved and no longer seen in the dropdown compartment. Another aspect of our attention was drawing attention to the effect of the buffer compartment. As the volume increases, the unstable region around $N_{\Delta h} = 1.1$and $N_{sub} = 0.9$ remains the same, even for very large volumes of this region for small volumes of buffer compartments in the stability maps. However, it is covered by other instabilities. Figure 8 shows the stability map for a system with a buffer size of $1m^3$, which is actually a thousand times the reference value. These instabilities are not dynamic, but they are known as leading instabilities. These instabilities remain constant when the volume of the buffer becomes large. Leading instabilities can be obtained using the mode equations of the previous sections. The linear fluctuation equation does not show any dependence on the buffer volume, so this unstable domain remains, even when the volume increases to a large value.

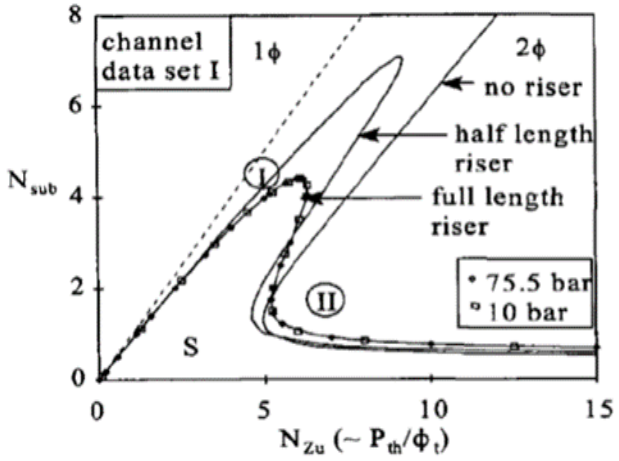

Figure 8: Stability map (Buffer compartment of 1 cubic meter)

Rising length

Van Braget (1998) examined the effect of rising length on the natural flow loop stability in a boiling water reactor. In Figure 9, a three-dimensional map of the neutral boundary is shown for three different lengths of the riser.

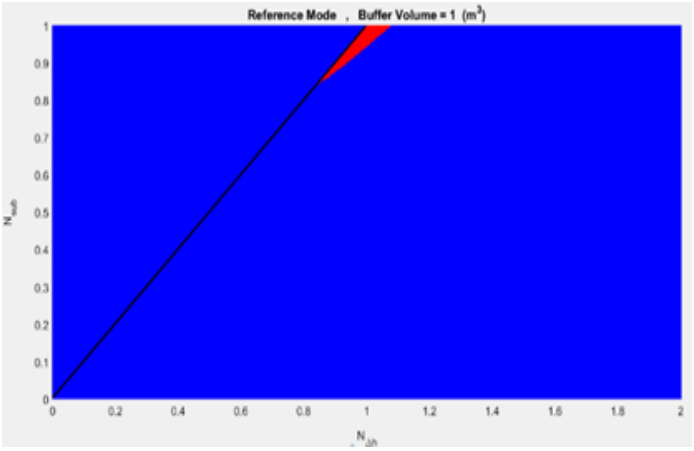

Figure 9 shows three neutral stability boundaries for a boiling water reactor with different riser ranges. Dimensionless numbers are comparable to the numbers used in our review. S refers to the stable region, and 1 and 2 refer to different types of dynamic instabilities. As the rising length increases, the system becomes more stable (Van Braget 1998).
The dimensionless numbers used in his study were similar to our dimensionless numbers, with the difference in a coefficient:

$$N_{Zu} = \frac{q' L_c}{\phi_t (h_g - h_f)} \frac{\rho_f - \rho_g}{\rho_g}, N_{sub} = \frac{h_f - h_{l_{C,i}}}{h_g - h_f} \frac{\rho_f - \rho_g}{\rho_g} \quad (35)$$

Subscript N_{Zu} is related to the vapor and the Subscript $N_{\Delta h}$ is related to the saturation fluid. *f* is comparable to g, because N_{Zu} is also proportional to the power on the mass flux (shown by red), and the sub-cool number increases when the enthalpy of the input (shown by red) decreases, similar to our study. Although the boiling water reactor with a fourth-generation water reactor, such as high-performance light water reactors, is different in the effect of the rising size, as in both of these, we have extreme density reduction, when the enthalpy increases, these two can be compared. As is shown in the figure above, type 1 instabilities appear when the riser is introduced to the system. These instabilities are due to the accelerating gravitational pressure (Van Braget,1998). As the rising length increases, the neutral stability boundary goes down in the stability map. Figure 10 shows the boundary of neutral stability for different rising lengths in this study. Comparison with Van Braget's map shows that the increase in the rising length has a similar effect on the system stability. As the rising length increases, the neutral boundary goes down in the stability map. When there are no risers, the neutral stability boundary goes to the right (similar to Van Braget's results in 1998), and only a small area remains due to leading instability (this will be discussed later in this section). When the rising length increases, type-1 instability predominates and leads to the stability boundary. Type 1 instabilities are explained in this way. Imagine a mass flux disruption is applied to the core input, say, a small increase. This results in less heat seeing the mass flux and, as a result, an enthalpy causes the lower output of the core (albeit assuming a constant input of the core). The resultant higher density in the outlet of the core and riser leads to a decrease in the drop in the gravitational pressure between riser and faller. Thus, mass flux rate decreases. Subsequently, the core gives more heat to the mass flow, so the enthalpy of the output increases. Thus, a precisely opposing process proceeds and leads to an increase in the mass flux rate (starting from the beginning of the path). These oscillations increase as the length of the rising length increases, because the pressure drop due to the gravity increases. When the amplitude of the oscillation increases over time rather than the decrease, it leads to instability. Consequently, the reduction of the stability boundary to increase the rising length indicates that type 1 instability plays an important role in the stability of the super-critical loop water flow.

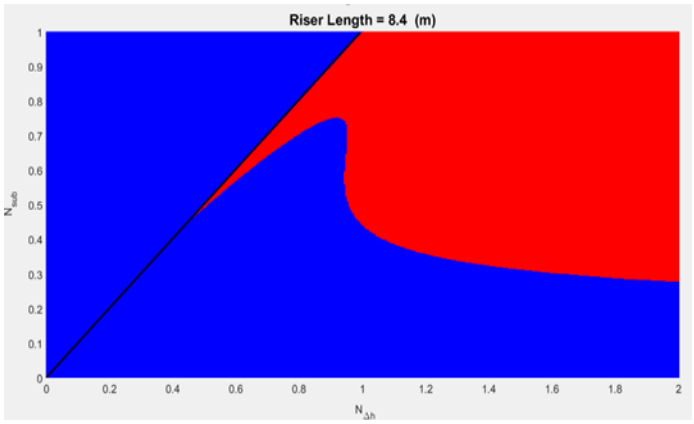

Figure 10: Stability map with different rising lengths

Improving the rising length evaluation

In the previous section, we saw that as the rising length increases, the stability decreases, as both areas of instability increase in size. Thus, we saw that the fluctuations of the density caused by both increases. The purpose of this is to express the difference between our findings and those of Van Braget. As the differences are in a region where instabilities are often due to friction, to understand the cause of the differences, we have to analyze the following instabilities:

$$\Delta P_{friction} = (\frac{fL}{D_H} + K)\frac{W^2}{2\rho} \qquad (36)$$

The frictional pressure drop can be calculated as follows. Here is a basic point that should be singled out. In the study we had done, all the parameters except one were changed in each node. Indeed, the hydraulic diameter was considered constant throughout the system. It is good to note that the hydraulic diameter directly affects the mass flux of the steady mode, and according to the following equations, which also affects the friction factor. Thus, changing the hydraulic diameter can affect the friction-induced instabilities and greatly affect $f = 0.316Re^{-\frac{1}{4}}$ and $Re = \frac{\bar{W}D_H}{A\mu}$. The constant consideration of it during loop leads to a lot of simplification, during which, one may not see a series of basic behaviors. Contrary to our study, Van Braget determined a particular hydraulic diameter for each particular model of his model. The difference is expected to be based on the difference in the hydraulic diameter selected. Indeed, the rising hydraulic diameter is much larger than the rest of the system. A large hydraulic diameter increases the volume (surface area ratio), so the gravitational force increases (friction ratio). Although it is not possible to say precisely, it seems that in the large hydraulic diameter, the inertia of gravity is more important than friction-induced instabilities. This means that the increase in the length of a large hydraulic divergence can lead to instability toward the type 1 region, without reducing the stability of the system (as seen in Braget). We consider the rising hydraulic diameter apart from the rest of the loop to confirm whether the expectation that different hydraulic diameter sizes are the reasons behind these contradictory results. The rising length, such as our calculations, varies for different values of the elevated hydraulic gauge. First, we assume different lengths (reference value 0.0056) for a diameter of 0.001 m.

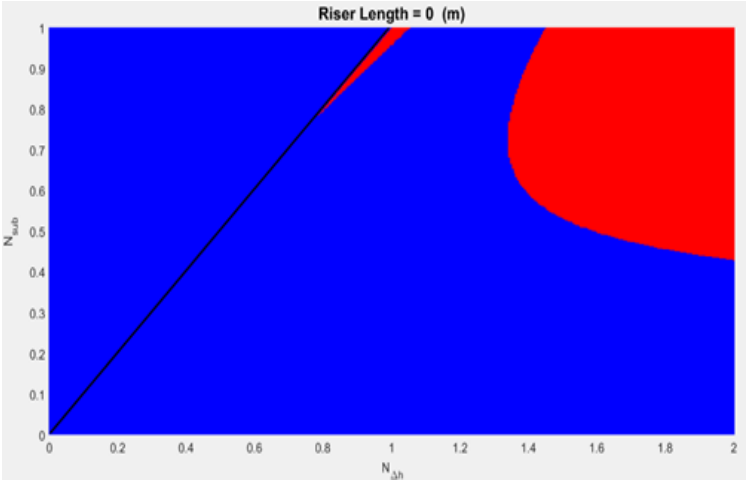

Figure 11: Stability map (the upper left side is related to the rising length 4.2, the upper right 12, and the lower figure is related to the rising length of 20)

Given the limitations we have for encoding, zero rising length is impossible in these cases.
Then, for a 0.01 meter diameter, we will increase the lengths to the varying degrees.

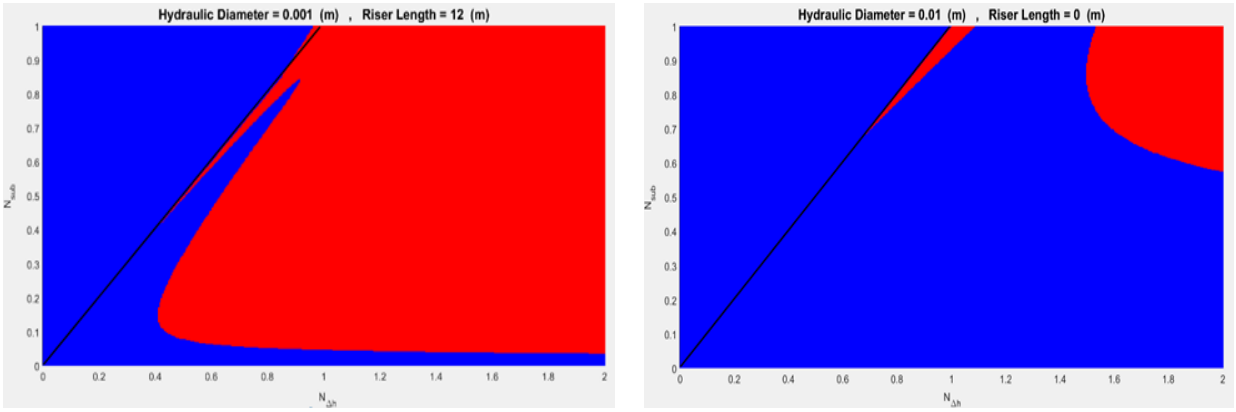

Figure 12: Stability map (upper left side is for rising length 0, rising length 12)

Finally, for the hydraulic diameter of 0.056 m, we assign different lengths to the riser. As explained in the texts above, the changes observed can explain the difference that was obtained with Van Braget's results.

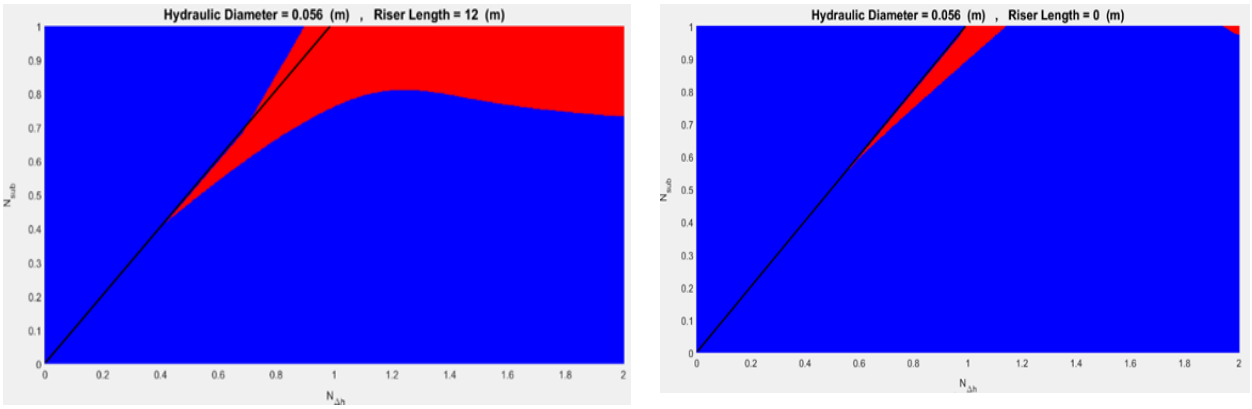

Figure 13: Stability map (rising length increases from top to bottom)

Core length and hydraulic diameter

The lengths of the core and the hydraulic diameter have opposite effects compared to the results obtained in Ortega Gómez (2009). He examines the design parameters for light water reactors with high pump performance. Indeed, his results show that the increase in the heated length and the reduction of the hydraulic diameter of the reactor has an effect on the incidence of this type of reactor. However, opposite results were achieved in this study. When the length of the core increased and the hydraulic diameter decreased, type 1 instability tended toward stability. However, the lower right side of the instability domain becomes more unstable (the area around $N_{sub} = 0.4$ and $N_{\Delta h} = 1.2$ in Figure 14). The down right side probably involves type II instability, as these are caused by friction (Van Braget ,1998). As is seen in the momentum issue, the friction becomes larger for the length of the core and the smaller hydraulic diameter. One has to note that the stability of the system depends on which part of the friction is most likely to increase.

The limitation on the entrance to the channel reduces in the increasing flow rate and has a stabilizing effect. The output limitation, on the other hand, has a destabilizing effect, because it reduces the flow rate and may change the phase by changing the flow (Boure & Bergles, 1973). Reducing hydraulic diameter leads to an increase in all parts of the friction due to the shear stress of the wall, but due to the lower density in the riser, the output friction increases the input friction more and the system becomes unstable (momentum equations). The same applies to the length of the core, as an increase along the core implies an increase in friction at Node 1. Friction in Node 1 can be considered as an output limitation because the flow in this node passes from a quasi-critical point. As the specific volume in Node 1 is greater than in Node 0, the friction in Node 1 is greater than in Node 0, so the system becomes more unstable. The stability map shows this point. They stated that higher frequencies appear in type 2 instability and lower frequencies in the type 1 instability region.

In this section, for specific hydraulic diameters, we examine the length of different cores.
First, we will examine the length of different cores for a hydraulic diameter of 0.001 m.

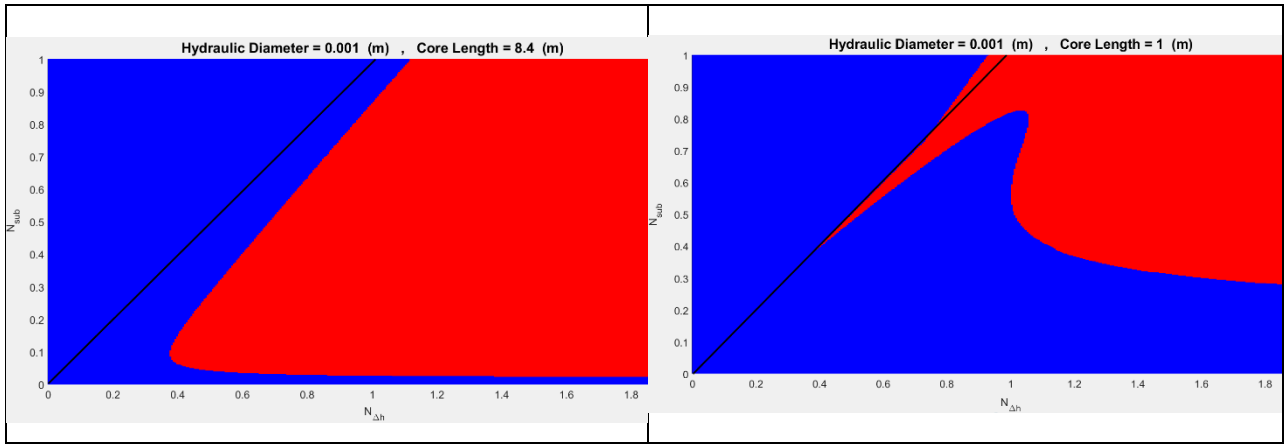

Figure 14: Stability map (we see the increase in core length, respectively)

Now, for a 0.01-inch hydraulic diameter, we will have a stability map for the different lengths of the core.

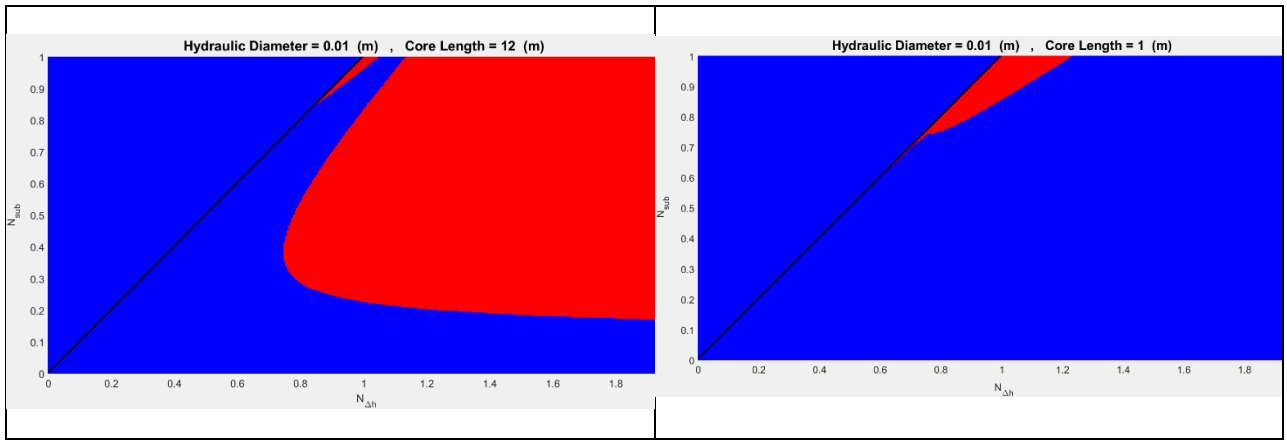

Figure 15: Stability map (the upper left side is the length of the core 1, the upper right 4.2, the lower left side 8.4 and the lower right side the core length 12)

Finally, we will have the stability map for the diameter 0.056 m.

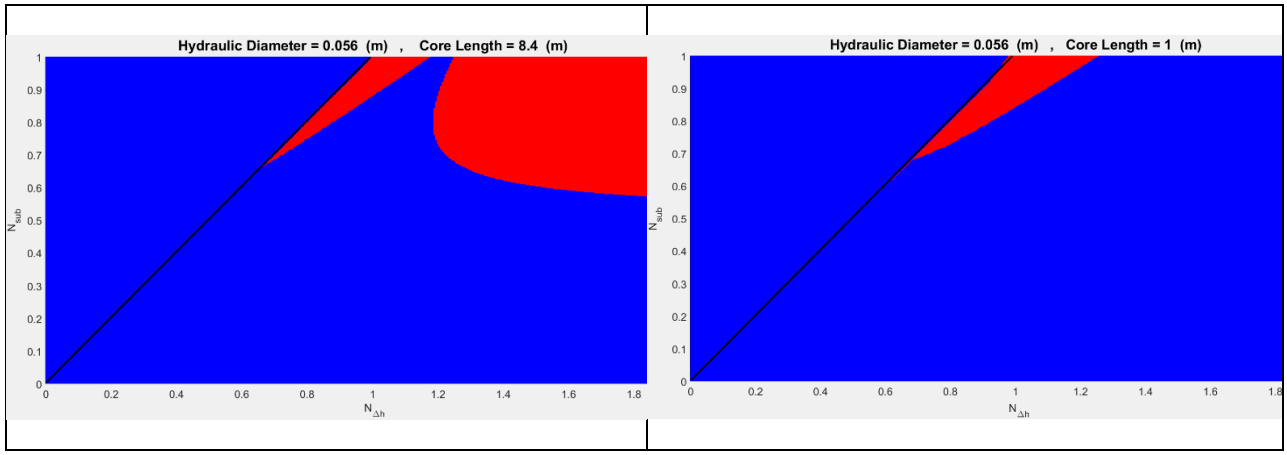

Figure 16: Stability map (we see an increase in core length, respectively)

Input and output limitations

According to the studies, the pressure drop coefficients have the same effect as those obtained from Ortega Gómez (2009). The input pressure drop coefficient of K_R has an ineffective effect and the coefficients of input pressure K_D and K_0 have a stabilizing effect. K_1 drop pressure coefficient in the super-critical model is zero, as the assignment of a value to it results in a discontinuous mass flux rate at $N_{sub} = N_{\Delta h}$. As the sub-critical model does not include this pressure drop coefficient, the mass flux rate for the super-critical model will be less than the mass flux rate for the sub-critical model. The pressure drop in the heavy liquid region has a stabilizing effect and the pressure drop in the fluid region has a destabilizing effect (Ortega Gómez, 2009). Both K_0 and K_D are present in super-critical water loop areas (Figure 17). The rising input pressure drop coefficient is considered as the output drop of the core output and is related to the low-density region. This pressure drop factor ultimately makes the system unstable.

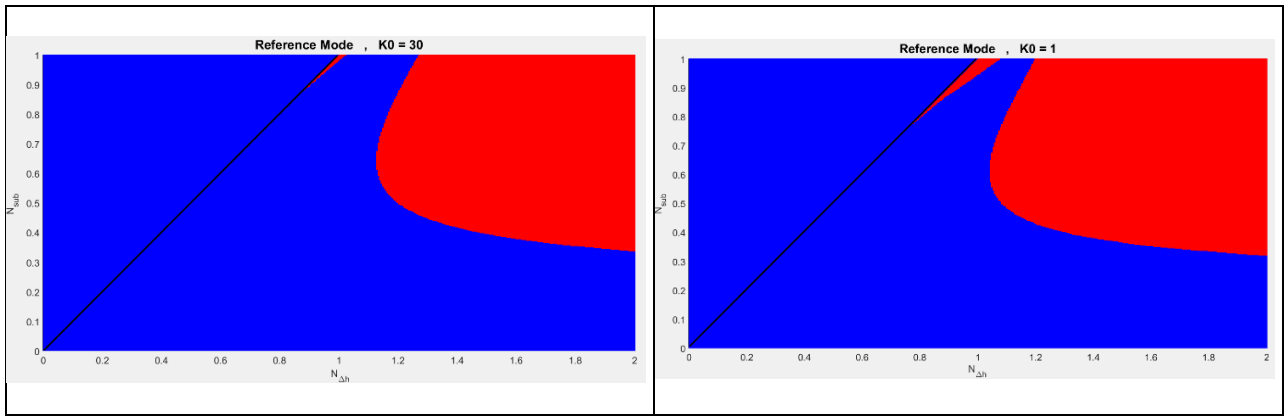

Figure 17: Stability map (constant coefficient increases, respectively)

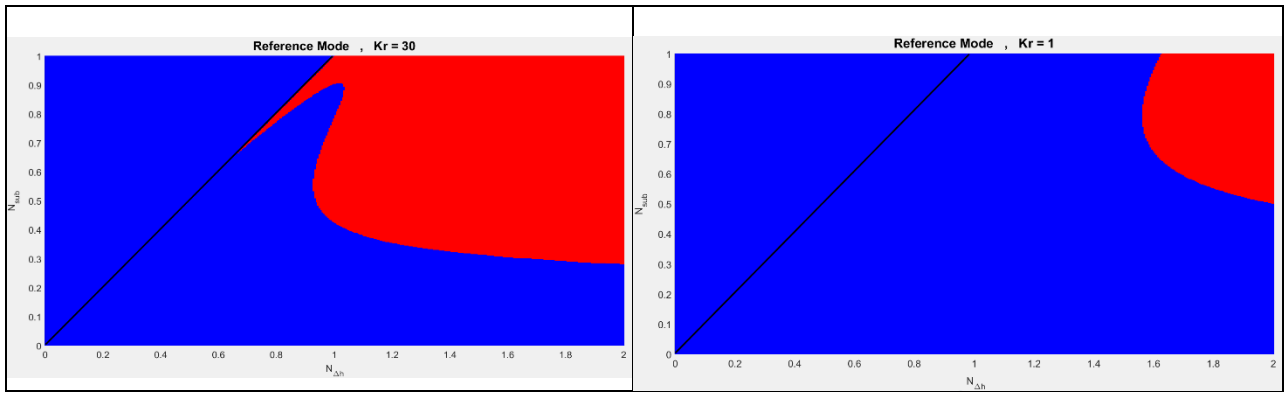

Figure 18: Stability map (constant coefficient of pressure drop increases, respectively)

According to the figures obtained, it is seen how the changes are. In the areas of high density, the increase of the pressure-drop coefficient has a positive effect on stability.

References

Boure, J. A., Bergles, A. E., & Tong, L. S. (1973). Review of two-phase flow instability. *Nuclear engineering and design*, *25*(2), 165-192.

Colombo, M., Cammi, A., Papini, D., & Ricotti, M. E. (2012). RELAP5/MOD3. 3 study on density wave instabilities in single channel and two parallel channels. *Progress in Nuclear Energy*, *56*, 15-23.

Ortega Gómez, T. (2009), Stability Analysis of the High Performance Light Water Reactor, Ph.D. dissertation, Institut für Kern- und Energietechnik

Rodríguez Cano, J. J., & de Amo, E. (2012). Taylor's Expansion Revisited: A General Formula for the Remainder. *International Journal of Mathematics and Mathematical Sciences*, *2012*.

van Bragt, D. D., & van der Hagen, T. H. (1998). Stability of natural circulation boiling water reactors: part I—description stability model and theoretical analysis in terms of dimensionless groups. *Nuclear Technology*, *121*(1), 40-51.

Vijayan, P. K., Sharma, M., Pilkhwal, D. S., Saha, D., & Sinha, R. K. (2010). A comparative study of single-phase, two-phase, and supercritical natural circulation in a rectangular loop. *Journal of engineering for gas turbines and power*, *132*(10).

Yu, J., Che, S., Li, R., & Qi, B. (2011). Analysis of Ledinegg flow instability in natural circulation at supercritical pressure. *Progress in Nuclear Energy*, *53*(6), 775-779.